Journal of Remote Sensing
A SCIENCE PARTNER JOURNAL

RESEARCH ARTICLE

Diurnal Carbon Monoxide Retrieval from FY-4B/GIIRS Using a Novel Machine Learning Method

Zhenxing Liang[1], Dasa Gu[1,2*], Mingshuai Zhang[3], Ning Yang[4], Chun Zhao[3,5,6], Rui Li[3], Qiaoqiao Wang[4], Yuxuan Ye[7,8], Jian Liu[9,10], Xin Li[1], Rui Liu[11], Yisheng Zhang[12], and Xiangyunong Cao[1]

[1]Division of Environment and Sustainability, Hong Kong University of Science and Technology, Clear Water Bay, Hong Kong SAR, China. [2]Guangdong-Hongkong-Macau Joint Laboratory of Collaborative Innovation for Environmental Quality, Hong Kong University of Science and Technology, Clear Water Bay, Hong Kong, China. [3]School of Earth and Space Sciences, University of Science and Technology of China, Hefei, China. [4]Institute for Environmental and Climate Research, Jinan University, Guangzhou 511443, China. [5]CAS Center for Excellence in Comparative Planetology, University of Science and Technology of China, Hefei, China. [6]Deep Space Exploration Laboratory, University of Science and Technology of China, Hefei 230026, China. [7]Key Laboratory of Regional Sustainable Development Modeling, Institute of Geographic Sciences and Natural Resources Research, Chinese Academy of Sciences, Beijing 100101, China. [8]College of Resources and Environment, University of Chinese Academy of Sciences, Beijing 100049, China. [9]School of Atmospheric Sciences, Sun Yat-Sen University, Zhuhai 519000, China. [10]College of Environment and Ecology, Taiyuan University of Technology, Jinzhong 030600, China. [11]Department of Geography, The University of Hong Kong, Hong Kong SAR, China. [12]School of Environmental and Municipal Engineering, Qingdao University of Technology, Qingdao 266520, China.

*Address correspondence to: dasagu@ust.hk

Citation: Liang Z, Gu D, Zhang M, Yang N, Zhao C, Li R, Wang Q, Ye Y, Liu J, Li X, et al. Diurnal Carbon Monoxide Retrieval from FY-4B/GIIRS Using a Novel Machine Learning Method. *J. Remote Sens.* 2024;4:Article 0289. https://doi.org/10.34133/remotesensing.0289

Submitted 21 February 2024
Revised 11 September 2024
Accepted 13 September 2024
Published 1 November 2024

Carbon monoxide (CO) is one of the primary reactive trace gases in the Earth's atmosphere and plays an important role in atmospheric chemistry. The Geostationary Interferometric Infrared Sounder (GIIRS) onboard the FY-4 series satellites is currently the only geostationary hyperspectral thermal infrared sensor capable of monitoring the unprecedented hourly CO concentrations in East Asia during both daytime and nighttime. In this study, we presented a radiative transfer model-driven machine learning approach to quickly convert CO spectral features extracted from FY-4B/GIIRS into CO total columns. We built machine learning models for land and ocean regions separately from July 2022 to June 2023, and these models reproduced more than 97.77% (land) and 98.49% (ocean) of the CO column variance in the training set. We estimated the absolute uncertainty of the retrieved CO column based on error propagation theory and found that it is dominated by GIIRS measurement noise. We compared the machine learning retrieval results with optimal estimation and ground-based Fourier transform infrared measurements, and the results reveal the consistent spatial distribution and temporal variation across these different datasets. Our results confirm that the machine learning method has the potential to provide reliable CO products without the computationally intensive iterative process required by traditional retrieval methods. The diel cycle and monthly variation of CO over land and ocean demonstrate the value of GIIRS in monitoring the long-range transport of anthropogenic pollutants and biomass burning emissions.

Introduction

Carbon monoxide (CO) is one of the primary reactive trace gases in the Earth's atmosphere, whose atmospheric concentration is maintained by surface emissions from incomplete combustion of fossil fuels in industry, traffic and domestic heating, or biomass burning, plus production through oxidation of methane and non-methane hydrocarbons in the atmosphere [1,2]. Additional minor sources of CO include ocean and vegetation [3]. Production of CO is balanced by removal mainly from the reaction with the hydroxyl radical (OH), the primary tropospheric oxidant, thus directly affecting the atmospheric oxidation capacity [4,5]. Atmospheric CO concentration is essential in air quality and climate because CO is a precursor of tropospheric ozone and carbon dioxide [2,6]. CO can also serve as a tracer for investigating long-distance transport of

pollutants due to its relatively long lifetime from weeks to months (e.g., [7]).

Several low-Earth orbit (LEO) nadir-viewing satellite instruments launched over the past 2 decades provide near-global measurements of CO vertical profile or total column based on its absorption of thermal or near-infrared (TIR or NIR) radiation [8,9]. These instruments and associated CO retrieval efforts include, but are not limited to, Terra/MOPITT (Measurement Of Pollution In The Troposphere) [10], Aqua/AIRS (Atmospheric Infra-Red Sounder) [11], Aura/TES (Tropospheric Emission Spectrometer) [12], MetOp/IASI (Infrared Atmospheric Sounding Interferometer) [13,14], Suomi-NPP/CrIS (Cross-track Infrared Sounder) [15,16], Envisat/SCIAMACHY (SCanning Imaging Absorption spectroMeter for Atmospheric CHartographY) [17,18], Sentinel-5P/TROPOMI (Tropospheric Monitoring Instrument) [19,20], and GOSAT-2/TANSO-FTS (Thermal And Near infrared Sensor for carbon Observations-Fourier Transform Spectrometer) [21]. MOPITT uses TIR or NIR radiation or both to retrieve the CO profile. The TIR-only retrieval is typically most sensitive to CO in the middle and upper troposphere, and when there is sufficient thermal contrast also sensitive to the lower troposphere. The TIR-NIR retrieval provides higher vertical resolution and features the greatest low-tropospheric sensitivity. The latter 3 instruments use NIR radiation, and the other sensors use TIR radiation. The operational products of the above instruments are all based on physical methods. The TIR instruments usually use the optimal estimation (OE) method, and NIR instruments use the OE, the differential optical absorption spectroscopy (DOAS) method or their variants. Specific retrieval details can be found in the above works and references therein. Under cloud-free conditions, the above LEO instruments can typically acquire near-global measurements of CO with a ground spatial resolution of ~5 to 22 km (AIRS has a coarser spatial resolution of ~45 km) at a temporal resolution of half a day to 5 d.

In June 2021, China launched an operational geostationary (GEO) orbit satellite, Fengyun-4B (FY-4B), equipped with a hyperspectral Geostationary Interferometric Infrared Sounder (GIIRS), which is the successor of the experimental satellite FY-4A launched in 2016 [22]. In June 2022, the FY-4B satellite and its ground application system entered trial operation and started providing observation data and application services to global users. By combining FY-4A and FY-4B, GIIRS can scan East Asia at a time resolution of about 1 h with a spatial resolution of 12 to 16 km at nadir. However, an experiment shows that the measurement performance of FY-4A/GIIRS in the long-wave channels is inconsistent with that of FY-4B by comparing measured and simulated radiances [23], which could raise questions about their compatibility for combination. So far, FY-4B/GIIRS is the only operational GEO hyperspectral thermal infrared instrument, with its mid-wave band (~1,650 to 2,250 cm^{-1} with a spectral resolution of 0.625 cm^{-1}) containing the sensitive intervals of CO. Therefore, GIIRS is valuable in diurnal CO retrieval with high temporal resolution.

Zeng et al. [24] recently retrieved the first CO at 2-h resolution for July 2022 from FY-4B/GIIRS based on the OE method, demonstrating the capability of GIIRS in observing the diurnal variation of CO in East Asia. OE is one of the most used physical methods in trace gas retrieval, which combines spectral measurements, prior state information, and corresponding uncertainty constraints and employs an iterative process to minimize the cost function between the measurements and the atmospheric state to infer an optimal solution [25,26]. OE can accurately retrieve trace gases with good prior knowledge, accurate radiative calibration, and radiative transfer simulation [27,28]. However, the iterative process is complex and computationally resource-intensive because each process needs to map the atmospheric state vector to the satellite measurement vector through the radiative transfer model (RTM). Another limitation of the OE method is that it yields back the a priori when the spectral signal of the target species is not strong enough [29], which is often the case with weak and broadband absorbers like the volatile organic compounds (VOCs) or low instrument sensitivity due to atmospheric conditions [30]. Furthermore, due to the contamination of the radiances in some GIIRS channels [23,31,32], and lack of analysis of the measurement performance of the adopted GIIRS spectral channels and necessary channel screening, the current OE CO product has a relatively noticeable latitudinal banding effects (i.e., deviations).

Machine learning (ML) methods have gradually been developed for fast satellite remote sensing retrieval [33,34]. Whitburn et al. [35] proposed the artificial neural network (ANN) method and subsequently applied it to ammonia retrieval using the hyperspectral range index (HRI) derived from IASI data. Then, the technique was gradually improved and applied to the retrieval of ammonia, methanol, formic acid, peroxyacetyl nitrate (PAN), acetone, acetic acid, isoprene, and ethylene from IASI and CrIS [30,36–41]. Although compared with the traditional OE method, ML has shortcomings in analyzing the uncertainty contribution sources and vertical sensitivity of the retrieval results, such methods reduce the importance of the forward model in retrieval by constructing the nonlinear relationship between the column and spectral index of the target species and are computationally efficient [30,35]. Another advantage of this method is that the temporal and spatial variation of the target gas concentration usually shows high agreement with the spectral index. HRI is a sensitive spectral index that quantifies the feature intensity of a target species in a specified continuous spectral interval by combining measurement covariance, spectral sensitivity to target species, and background measurement [42]. However, like the OE approach, HRI might be prone to false detection when a major spectral interference (e.g., another trace gas and water vapor or emissivity features) overlaps with the absorption band of the target species [37,43]. Furthermore, abundant surface and atmospheric sources and relatively long lifetimes produce a relatively uniform CO background column, which makes it inconvenient to select the satellite background observation (where no target trace gas appears) required in HRI.

This study expects to use the ML approach to retrieve long-term diurnal CO columns quickly and reliably from FY-4B/GIIRS and weaken the band deviation in the current OE product. Compared with HRI, the brightness temperature difference (BTD) between the absorption peak and valley of the target species can be regarded as a relatively conservative spectral index, which is also widely used to characterize the distribution of various trace gases [44–49]. The abundant sources, relatively long lifetime, and strong absorption in several thermal infrared channels allow atmospheric CO columns to produce considerable brightness temperature contributions. Therefore, we introduce the use of the BTDs at carefully selected multiple spectral channels as the spectral index, construct a representative training set with accurate radiative transfer simulation, and use ML methods to convert the spectral index into CO columns. It is also the first study where CO columns retrieved from GIIRS are compared to co-located high-quality ground-based solar absorption Fourier transform infrared (FTIR) measurements.

The content is structured as follows: The "Datasets" section describes the sources and roles of data needed in the retrieval and evaluation. The "Methodology" section describes the ML framework and the technical details. The "Results and Discussion" section shows the retrieval results, compares them with OE products, evaluates them with ground-based measurements, and discusses the advantages of GIIRS. Finally, we conclude in the "Conclusions" section.

Materials and Methods

Datasets

FY-4B data

GIIRS is carried on the FY-4 satellite series in GEO orbits about 36,000 km above the equator [22]. FY-4B/GIIRS completes 12 full scans per day over the observation region (as shown in Fig. S1) with a spatial resolution of 12 km at nadir. The spectral range of FY-4B/GIIRS includes mid-wave (MWIR; 1,650 to 2,250 cm^{-1}) and long-wave infrared (LWIR; 680 to 1,130 cm^{-1}), with a spectral resolution of 0.625 cm^{-1}. The experiment results of blackbody calibration in a laboratory thermal vacuum tank conducted by Li et al. [50] show that the noise equivalent differential radiance of FY-4B/GIIRS in the LWIR band is less than 0.5 mW/(m^2·sr·cm^{-1}) and that in the MWIR band is lower than 0.1 mW/(m^2·sr·cm^{-1}). The average radiometric calibration difference in the LWIR band is improved from 1 K to 0.2 K after the nonlinearity correction, and that in the MWIR band also meets the 0.7 K index requirement in the dynamic range of 260 to 315 K, which is comparable to existing infrared sounders.

FY-4B/GIIRS provides level 1 data from June 2022, and this study uses the level 1 MWIR radiation data of FY-4B/GIIRS to extract the spectral feature of CO. The corresponding observation geometry is used in the RTM simulation and participates in ML retrieval as the auxiliary parameter. We removed the invalid GIIRS measurements and filtered data with quality assessment scores in the level 1 product less than 60. The high-resolution (4 km) cloud mask (CLM) product from the Advanced Geostationary Radiation Imager (AGRI) onboard FY-4B was then used to screen clear-sky measurements [51,52]. Specifically, we matched the surrounding CLM products for each GIIRS footprint and kept GIIRS measurements with at least 80% of the CLMs marked as clear or probably clear. All the above FY-4 data are available at http://satellite.nsmc.org.cn/PortalSite/Data/Satellite.aspx?currentculture=en-US.

Auxiliary data

This study uses atmospheric pressure, temperature, water vapor profile, surface temperature and pressure, 2-m temperature, and 10-m wind speed from the European Centre for Medium-Range Weather Forecasts (ECMWF) ERA5 and the monthly infrared land surface emissivity database from the University of Wisconsin-Madison (UOW-M) in the RTM to simulate GIIRS infrared radiation, and part of them also participated in ML retrieval. The temporal resolution of ERA5 is 1 h, and the spatial resolution is 0.25° [53]. The UOW-M emissivity data have 10 wavenumbers from MWIR to LWIR [54], and interpolation was performed here to derive the emissivity in the needed channels. These auxiliary data were spatiotemporally sampled to match the GIIRS observations. The ERA5 data are available at https://www.ecmwf.int/en/forecasts/datasets/reanalysis-datasets/era5. The UOW-M emissivity data are available at https://cimss.ssec.wisc.edu/iremis/.

Intercomparison CO dataset

Zeng et al. [24] retrieved the CO for July 2022 from FY-4B/GIIRS based on the OE method and compared the CO columns with MetOp-B/IASI L2 CO total column products. IASI is a LEO satellite sensor with high radiometric performance [55], stable retrieval algorithms [13], and mature products [9,27,56–60]. In this study, the above GIIRS-OE CO columns from July 2022 were used to compare with the GIIRS-ML retrieval results. The MetOp-B/IASI CO products were used to evaluate the first monthly variation of GIIRS-ML CO. The GIIRS-OE CO data are available at https://doi.org/10.18170/DVN/M7DKKL. The IASI CO products are available at https://iasi.aeris-data.fr/.

Ground-based FTIR measurements

This study uses CO products provided by 2 ground-based FTIR sites (Fig. S15) within the GIIRS coverage region to evaluate the CO columns retrieved from GIIRS. These 2 FTIR sites belong to the Total Carbon Column Observing Network (TCCON) [61–63]. One is located in Hefei, China [64,65], and the other is in Saga, Japan [66,67]. TCCON uses solar absorption spectroscopy in the NIR region and adopts a nonlinear least-squares spectral fitting algorithm (same as OE) to iteratively retrieve the scaling factor of the prior vertical profile until the forward simulated spectrum best fits the observed spectrum. The scaled prior profile is integrated over the vertical height to generate the vertical column density of the target gas, which is then divided by the dry air column density to derive the final column-average dry mole fractions (XCO). The accuracy of XCO retrieved by the latest version of the algorithm (called GGG2022) has increased from 4% to 2% compared with the older version (GGG2014) [61,62]. More information about TCCON is available on its official website and in references (http://www.tccon.caltech.edu/).

Methodology

The GIIRS-ML approach first uses RTM to simulate the radiances that GIIRS would receive under different observation angles, atmosphere-surface state parameters (i.e., auxiliary parameters), and various CO columns, and then extracts the simulated spectral features of CO (i.e., BTD). The relationship between the CO column and its generated BTD is a complex function influenced by auxiliary parameters that affect radiative transfer. So, ML is used here to construct the nonlinear relationship between the RTM-simulated BTD, the major auxiliary parameters (detailed in the "Training set preparation" section), and the CO columns. Finally, the trained ML model converts the GIIRS-calculated BTD and corresponding auxiliary parameters into the CO columns.

This section describes the steps as shown in Fig. 1 for retrieving the CO total column from FY-4B/GIIRS in detail, including RTM simulation, gas spectral sensitivity analysis, GIIRS spectral channel selection and CO spectral feature extraction, the representative training set construction, ML training and evaluation, and retrieval uncertainty estimation and post-filtering. We show the necessary figures in this section.

RTTOV and spectral sensitivity analysis

The RTM used in this study is RTTOV (Radiative Transfer for TOVS), which is a very fast RTM that can be used to simulate visible, infrared, and microwave downward-viewing satellite radiometers, spectrometers, and interferometers [68,69]. RTTOV has been used as the forward operator in a series of trace gas retrieval work, such as the CO, methanol, methane, ozone, and

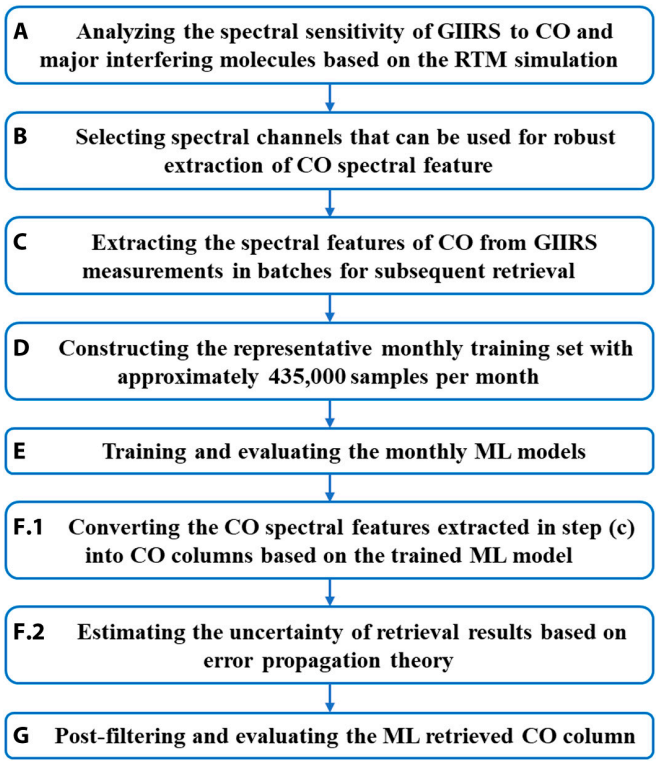

Fig. 1. A flowchart to illustrate the main steps of the methodology. The CO column retrieval (F.1) and uncertainty estimation (F.2) are performed simultaneously in the code.

water vapor, retrieved from IASI by the Rutherford Appleton Laboratory (RAL) space remote sensing group [70]. RTTOV characterizes sensor-specific measurements through its pre-generated coefficient files, and the FY-4B/GIIRS coefficient file is used here. The simulation error of RTTOV is characterized by comparison with an accurate line-by-line RTM and is involved in calculating retrieval uncertainty in the following section. More information is available at https://nwp-saf.eumetsat.int/site/software/rttov/.

Selecting spectral channels with as few interfering species effects as possible is essential for reliable CO retrieval. The MWIR band of FY-4B/GIIRS includes the strong absorption spectral interval of CO (~2,040 to 2,230 cm^{-1}), where the major interfering molecules include water vapor, N_2O, CO_2, and O_3. Figure 2A shows the spectral sensitivity of each trace gas calculated from RTTOV simulated brightness temperatures. There are substantial influences of water vapor, O_3, and CO_2 in the interval of ~2,040 to 2,143 cm^{-1} and that of N_2O in ~2,181 to 2,230 cm^{-1}. Therefore, in CO thermal infrared retrieval, the shaded interval (~2,143 to 2,181 cm^{-1}) is common to avoid the influence of other molecules except for water vapor. We calculated the difference in sensitivity to CO and interfering molecules between each pair of spectral channels in the shaded interval, as shown in Fig. 2B. Then, based on the principle of being sensitive to CO and insensitive to interfering molecules, we screened some spectral channel combinations composed of CO absorption peaks and valleys, as shown in Fig. 2C. These combinations can theoretically be used to extract the spectral features of CO. In addition, the interference between these channels mainly comes from water vapor, so several spectral channel combinations of water vapor were also screened out to consider its influence during retrieval.

GIIRS spectral channel selection and feature extraction

Whether the channels determined by the above RTTOV simulation are suitable for actual GIIRS measurements depends on the influence of interfering species and is closely related to the instrument measurement performance. Figure S2 shows the spectral features (i.e., BTDs) extracted from one peak channel (2,150.625 cm^{-1}) and each valley channel, where many BTDs exist banding effects and are more significant at the latitude bands scanned by the instrument and over the ocean. That is due to the contamination in the level 1 radiance of some GIIRS channels mentioned in the introduction and may also be due to the accumulation of dual-channel measurement errors when calculating BTD. Therefore, if we do not perform measurement performance analysis and necessary post-filtering of the GIIRS spectral channels, the retrieved gases may have apparent banding effects. Through visual analysis of all BTDs, we finally identified several channel combinations that can reliably extract the CO spectral features and weaken banding effects (Fig. S3).

Theoretically, an average value calculated using multiple valley channels provides a more robust characterization of the background spectrum, and the same principle applies to the peak channels [45,48]. After many experiments on channel averaging, corresponding ML model training, and retrieval (as shown in Fig. S4), we determined to use the brightness temperature at the absorption peak channel (2,154.375 cm^{-1}) and the average brightness temperature at the valley channels (2,143.125, 2,159.375, and 2,166.875 cm^{-1}) to extract the spectral features of CO (as shown in Fig. 3A). In Fig. 3A, anomalously high values occur in the boxed region A, which may be caused by the larger satellite viewing angles (Fig. 3C) with longer radiation propagation path and more disturbances. These anomalously high BTDs are also sparsely ground-sampled, and if they produce anomalous CO columns in the retrieval, the post-filtering can be easily performed according to the viewing angle. In the boxed region B, there are also high values, which should be caused by the surface emissivity (Fig. 3D) or thermal contrast (Fig. 3E), as the nadir thermal infrared instruments usually have higher sensitivities to the target gas at high thermal contrasts [71]. When these auxiliary parameters are considered in the ML model, these high BTD values map to the normal CO columns.

Except for the boxed regions A and B, in the hotspot regions usually densely populated by human activities (as shown in Fig. S5), such as the Sichuan Basin, the North China Plain, northeast China, Primorye Russia, northern India, and Pakistan, high BTD values correspond to high CO columns (Fig. 3B). In contrast, the relatively lower BTD values in southeast China and Southeast Asian countries (e.g., Vietnam and the Philippines) correspond to lower CO columns. In the Qinghai–Tibet Plateau region of China, the extremely low BTD values correspond to relatively uniform CO background columns and high altitudes. These performances illustrate that the spectral features calculated directly from the GIIRS measurements can characterize the CO distribution and column variation (except in regions strongly influenced by surface emissivity or viewing angle). In addition, related gas retrieval works usually input water vapor reanalysis data into the ML models to account for potential weak water vapor interference. Here, we replace the reanalysis data with water vapor spectral features extracted directly from GIIRS (Fig. 3F) to reduce the retrieval error and uncertainty.

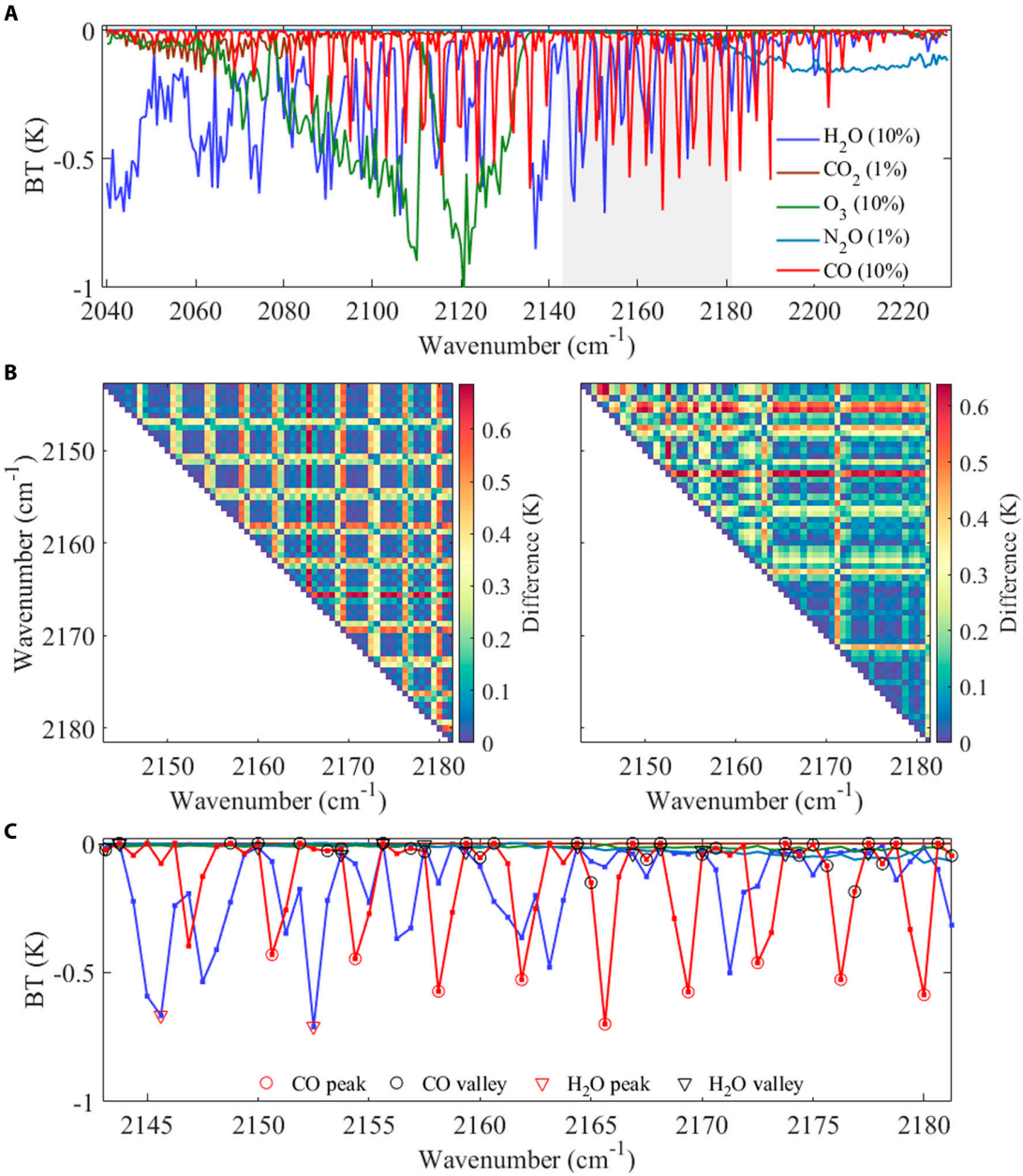

Fig. 2. Spectral sensitivity analysis and channel selection of CO. (A) Spectral sensitivities of CO and major interfering molecules (i.e., water vapor, N_2O, CO_2, and O_3), calculated from the change of RTTOV simulated brightness temperature produced by adjusting the column of each gas. The proportions of column adjustment marked in the legend are approximately their retrieval accuracy requirements. (B) Differences in sensitivity to CO (left panel) and interfering molecules (right panel) between each pair of channels in the shaded interval of (A). (C) The screened absorption peak and valley channels for CO and H_2O, and their combinations might be used to extract their spectral features.

Training set preparation

The performance of ML retrieval depends heavily on the quality of the training set, which should be as comprehensive and representative as possible [30]. Theoretically, all parameters that affect the radiative transfer simulation and spectral feature should be part of the training set, but the data dimension is huge and requires intensive computing resources. Therefore, only the spectral features of the CO and major auxiliary parameters are involved in the input parameters of the ML model, and the predicted output of ML is the CO column. These auxiliary parameters include spectral features of water vapor, satellite angles (zenith angle and azimuth angle), solar angles (zenith angle and azimuth angle), thermal contrast, surface pressure, surface skin temperature (sea surface temperature for ocean), and surface spectral emissivity. In this study, the land surface spectral emissivity was calculated from the UOW-M emissivity database. The surface spectral emissivity of the ocean can be characterized as a function of observation angle and wind speed [72], so we input the latter 2 directly into the model.

When constructing the training set, we extracted all the auxiliary parameters corresponding to all GIIRS cloud-free observations during the daytime and nighttime each month from July 2022 to June 2023 and then performed spatiotemporal regular sampling. Specifically, given the importance of thermal contrast to the instrument's sensitivity, we used thermal contrast as the flag to process each 0.5 × 0.5° grid. We first sorted the thermal

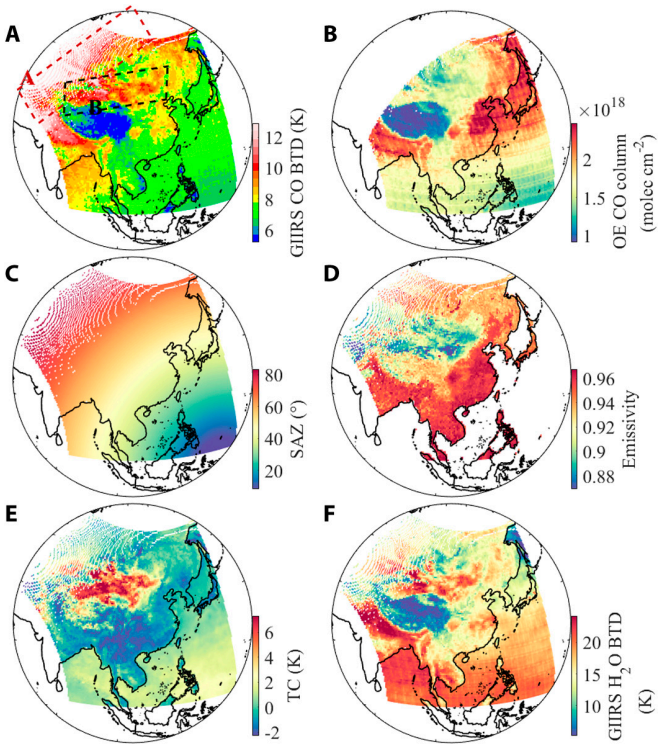

Fig. 3. Analysis of CO spectral features extracted from GIIRS measurements and major influencing factors in July 2022. (A) CO spectral features extracted directly from all GIIRS cloud-free measurements during daytime and nighttime based on the brightness temperature at the absorption peak channel (2,143 cm^{-1}) and the average brightness temperature at the valley channels (2,143.125, 2,159.375, and 2,166.875 cm^{-1}). Here, we adjust the color bar to highlight key information. (B) CO total column in the same month retrieved by Zeng et al. [24] based on the OE method. (C) Satellite zenith angles. (D) Surface emissivity calculated from the average of wavenumbers used in (A). (E) Thermal contrast (i.e., the temperature difference between the surface and the 2-m overlying layer). (F) Spectral features of the water vapor, calculated from the water vapor absorption peak (2,152.5 cm^{-1}) and valley channels (2,153.75 and 2,164.375 cm^{-1}). The above maps are monthly averages drawn at a spatial resolution of 0.5 × 0.5°.

contrast in each grid, saved the position index, and retained the maximum and minimum values. Then, we sampled the remaining samples at equal intervals to keep a constant ratio of the numbers. Finally, we extracted other corresponding auxiliary parameters according to the position index. Furthermore, we ensured that the number of samples obtained per unit time resolution was consistent to prevent the training set from overly representing a specific period. Such regular sampling ensures that samples can represent the measurement conditions of GIIRS while reducing data redundancy and improving the efficiency of ML training. Then, we assigned different CO profiles taken from random scaling of the reference profile to the representative auxiliary parameters and input them into RTTOV to simulate and generate a wide range of BTDs with various CO columns. The reference profile of CO was taken from the spatiotemporal average of the EAC4 monthly averaged fields in the study region in 2021 (as shown in Fig. S6) [73].

ML training and evaluation

After constructing the above RTTOV-derived training sets, we used the random forest (RF) method to build nonlinear relationships between input and output parameters each month. RF uses randomly selected training samples and subsets of variables to generate multiple decision trees that comprehensively determine the model output [74]. RF can successfully handle high-dimensional data and multicollinearity and only needs to adjust 2 parameters when training the model [33]. Since land and ocean have different surface properties, such as temperature and emissivity, related research has also shown that training separate ML models for land and ocean observations improves training performance for both groups [75]. In addition, there are large differences in observation conditions in different months. For example, favorable observation conditions in summer correspond to larger thermal contrast and lower measurement noise, while the opposite is true in winter. Therefore, we trained the monthly RF models separately for land and ocean, and then selected the corresponding models based on land and ocean markers and months during retrieval.

In the RF method, 2 parameters need to be set when generating forest trees: the number of decision trees (N_{tree}) and the number of variables to be selected and tested for optimal segmentation of growing trees (N_{try}) [33]. The latter is usually set to the square root of the number of input variables. We used 10-fold cross-validation to evaluate the performance of the RFs under different N_{tree}. Specifically, the training set was randomly divided into 10 parts, 9 of which were taken each time to train the model, and the remaining one was predicted. The control experiments in Fig. S7 show that with the increase in N_{tree}, the model R^2 increases and the root mean square error (RMSE) decreases and then gradually reaches a stable state with minimal fluctuations. In this study, N_{tree} was set to 200. We also used the mean relative error of the predicted columns ($\hat{y}$) over the trained columns y to evaluate the relative uncertainty of the model. The equation for calculating the mean relative error within each unit grid is as follows, where n is the number of columns in the grid [35]:

$$\overline{\text{Error}} = \frac{1}{n}\sum_{k=1}^{n}\left|\frac{\hat{y}_k - y_k}{y_k}\right| \times 100 \quad (1)$$

In July 2022, the coefficients of determination (R^2) between the training CO column and the RF-predicted CO column reach 0.995 and 0.989 over land and ocean, respectively (Fig. 4A and C), and the relative uncertainty of the model is generally less than 10% at columns greater than 0.5×10^{18} molecules/cm^2 over land and ocean [as shown in the 2-dimensional (2D) error plots Fig. 4B and D]. These two 2D error plots also show that the model's relative error increases at lower background columns, where the BTDs produced by the columns are closer to the detection threshold of the instrument. In Fig. 4E, the RF model outputs the expected relative importance of each parameter, i.e., the CO spectral feature dominates the model, and the satellite zenith angle also plays an important role. In addition, the importance of CO spectral features over the ocean is more significant than that over land. From July 2022 to June 2023, the performance of the RF model on the training set in each month is shown in Table S1. The performance of the RF model decreases slightly in the colder months due to unfavorable observation conditions, but overall performs well in all months, with R^2 larger than 0.97 and 0.98 over the land and ocean even in the coldest month (January 2023).

Retrieval uncertainty estimation and post-filtering mechanism

The absolute uncertainty for each retrieved CO column over land and ocean (S_{land} and S_{ocean}) was estimated by propagating the uncertainties of the input parameters in RF retrieval [35]:

$$s_{Land}=\sqrt{\left(\frac{\partial CO}{\partial BTD_{CO}}\right)^2\left(s^2_{BTD_{CO}}+s^2_{RTTOV_{CO}}\right)+\left(\frac{\partial CO}{\partial BTD_{H_2O}}\right)^2\left(s^2_{BTD_{H_2O}}+s^2_{RTTOV_{H_2O}}\right)+\left(\frac{\partial CO}{\partial TC}\right)^2 s^2_{TC}+\left(\frac{\partial CO}{\partial T_{skin}}\right)^2 s^2_{T_{skin}}+\left(\frac{\partial CO}{\partial SP}\right)^2 s^2_{SP}+\left(\frac{\partial CO}{\partial Se}\right)^2 s^2_{Se}} \quad (2)$$

$$s_{Ocean}=\sqrt{\left(\frac{\partial CO}{\partial BTD_{CO}}\right)^2\left(s^2_{BTD_{CO}}+s^2_{RTTOV_{CO}}\right)+\left(\frac{\partial CO}{\partial BTD_{H_2O}}\right)^2\left(s^2_{BTD_{H_2O}}+s^2_{RTTOV_{H_2O}}\right)+\left(\frac{\partial CO}{\partial TC}\right)^2 s^2_{TC}+\left(\frac{\partial CO}{\partial T_{skin}}\right)^2 s^2_{T_{skin}}+\left(\frac{\partial CO}{\partial SP}\right)^2 s^2_{SP}+\left(\frac{\partial CO}{\partial WS}\right)^2 s^2_{WS}} \quad (3)$$

where BTD_{CO} is the uncertainty of CO spectral feature, calculated as the average of the measurement noise equivalent temperature difference (NEdT) of the CO spectral channels used in BTD. $RTTOV_{CO}$ represents the mean simulation uncertainty of RTTOV in the above CO spectral channels. BTD_{H_2O} and $RTTOV_{H_2O}$ represent the instrument measurement noise and RTTOV simulation uncertainty at the water vapor spectral channels. S_{TC} and S_{Tskin} represent the uncertainty of thermal contrast and surface temperature and were set to 1 K, referring to Whitburn et al. [35]. S_{SP} is the uncertainty of ERA5 surface pressure set to 3 hPa [76]. S_{Se} is the uncertainty of the surface emissivity set to 0.01. S_{WS} is the uncertainty of the wind speed and set to 2 m/s [77]. The uncertainty of the satellite observation geometry was negligible. The results in Fig. S8 show that the uncertainty contributed by NEdT is usually more than 90% of the total uncertainty, indicating that the absolute uncertainty in the retrieved CO is dominated by instrument measurement noise. Figure S9 shows the absolute uncertainties of the retrieved columns for each month. It is obvious that under unfavorable observation conditions in the colder months from December 2022 to February 2023, the retrieval uncertainties are larger than in warmer months. Moreover, these regions with poor retrieval performance are mostly located in high-latitude areas with large GIIRS observation angles, high measurement noise, and sparse sampling, as well as in the high-altitude CO background regions of the Tibetan Plateau.

To determine a robust post-filtering basis, we observed thousands of the retrieved columns, uncertainties, and multiple influencing factors corresponding to GIIRS unit time observations in 4 representative months (one example in Fig. S10). We first used NEdT/BTD less than 10% as a strict basis and then filtered out those extremely cold observations with surface temperatures less than 273.15 K. Additionally, we made a mask file in Fig. S11 to filter out those sparsely sampled measurements. Figure S12 shows the performance of the post-filtering mechanism during the daytime and nighttime in each month. Specifically, the filtered number during the nighttime is larger than in the daytime and winter than in summer. In January 2023, the coldest month, nearly 40% of the retrieval results were filtered due to the strict thresholds, but most of these removed measurements were not in hotspots.

Results and Discussion

This section compares GIIRS-ML retrieval results with the OE method and performs the first evaluation of GIIRS CO with high-quality ground-based FTIR measurements. Note that since the CO profile has different action mechanisms in OE and ML methods, we usually call it the prior profile in OE and the reference profile in ML. We discuss the consistency and differences between the different products and point out ways to improve ML products further in the future. We also discuss the advantages of GIIRS in monitoring CO emissions and long-range transport by drawing the diel cycle of the GIIRS-ML CO column and its monthly variations for a whole year from July 2022 to June 2023.

Comparison of CO between ML and OE method

Zeng et al. [24] carried out the spatial and temporal comparisons between the GIIRS-OE CO column and the IASI CO product and showed good agreement between them. Here, we select the same regions and periods as in the above comparisons to compare the GIIRS-ML and GIIRS-OE CO columns. When comparing products from different sensors or algorithms (e.g., products A and B), it is usually best to consider the impact of different profiles and average kernels to make a proper comparison, as shown in the following equations [78]:

$$x^A_{adj}=x^A_{ret}+\left(AK^A-I\right)\left(x^A_a-x^B_a\right) \quad (4)$$

$$x^B_{\text{smooth}}=x^B_a+AK^A\left(x^B_{\text{ret}}-x^B_a\right) \quad (5)$$

where x is the CO concentration profile whose dimension is equal to the number of retrieved pressure levels (N) or the CO partial column profile whose dimension is equal to the number of layers ($M = N - 1$) and AK is the average kernel matrix ($N \times N$ or $M \times M$), representing the retrieved state's sensitivity to the true state. The dimensions depend on whether the product provides concentration profiles or partial column profiles. Equation 4 first uses a profile in product B to adjust the CO retrieved in product A. Then, Eq. 5 uses the average kernels in product A to smooth the CO retrieved in product B.

Figure 5A and B compares GIIRS-ML and GIIRS-OE columns in 2 daytime and nighttime scenes on 2022 July 7. The GIIRS-ML and GIIRS-OE columns show the same CO source regions, an anthropogenic emission source in the North China Plain, and a natural wildfire emission source in Siberia. In addition, the GIIRS-ML CO column during daytime over urban areas in northern India is slightly higher than that of GIIRS-OE. The scatterplots also show good agreements between GIIRS-ML and GIIRS-OE CO columns during daytime and nighttime. We performed various tests to discuss the impact of different profiles and average kernels, as shown in Figs. S13 and S14.

The results show that in trace gas retrieval, the profiles used in the OE or ML method have important impacts on the retrieval, and it is essential to introduce the average kernel in ML to evaluate the retrieval quality. The availability of average kernels has always been one of the greatest strengths of OE methods, while

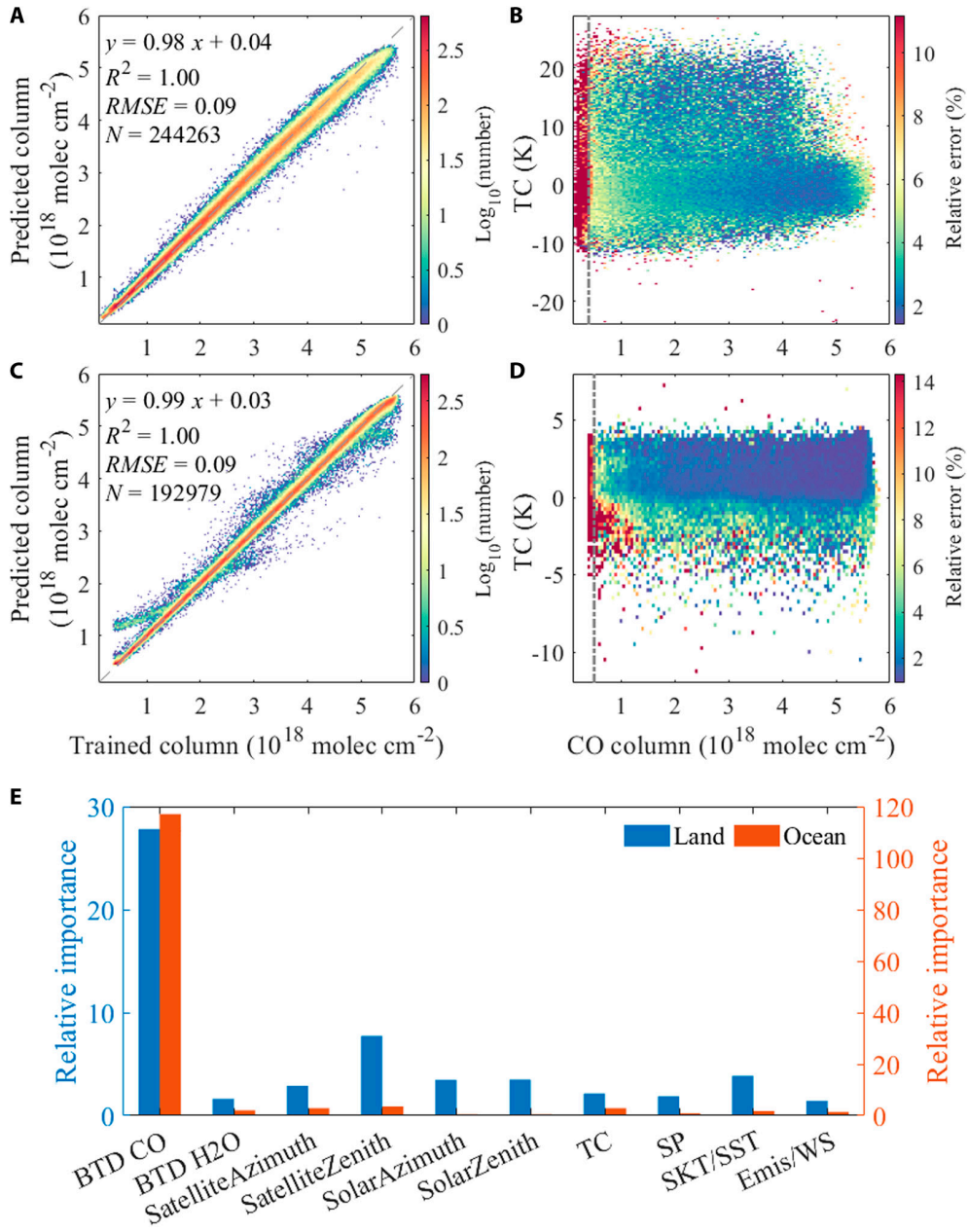

Fig. 4. Performance of the RF model on the training sets over land and ocean in July 2022. (A and C) Relationships between the trained and RF-predicted CO columns over land and ocean, respectively. (B and D) Relative uncertainty of the RF model in the unit TC and Column grid (0.25 K and 5×10^{16} molecules/cm^2) over land and ocean, respectively. The 2 grey dotted lines in (B) and (D) represent the marking lines for the CO column of 0.5×10^{18} molecules/cm^2. (E) Relative importance of input parameters in the RF model over land and ocean. The relative importance here indicates how each input parameter improves the model's prediction error. The higher the value, the greater the contribution of this parameter to the model's prediction results. The left *y* axis represents land, and the right *y* axis represents ocean.

the lack of average kernels is a major drawback of ML. Until a recent trace gas retrieval work, formulas for calculating average kernels in ML were systematically derived, which can be used to undo the effect of the profile shape assumption of the retrieval [79]. Therefore, the ways we are considering to improve the ML algorithm include selecting the optimal reference profile shape for different regions based on historical data and introducing average kernels.

For the comparison of time series in Fig. 5C, we refer to the 4 representative regions (as shown in Fig. S15) delineated by Zeng et al. [24], among which the North China Plain and northern India represent anthropogenic source regions with persistent high CO emissions, Mongolia represents the CO background region, and the Eastern China Sea represents the ocean. During the daytime and nighttime, the GIIRS-ML and GIIRS-OE columns in all 4 regions show consistent daily variabilities, reflecting that both methods can capture CO information from GIIRS. Except for the differences in a few days in northern India that lead to low correlation coefficients between the 2 datasets, the correlation coefficients in other regions and times are higher than 0.61, especially in the East China Sea, where the correlation coefficients reach 0.96 and 0.94 during the daytime and nighttime, respectively. The differences between the GIIRS-ML and GIIRS-OE columns as a proportion of the

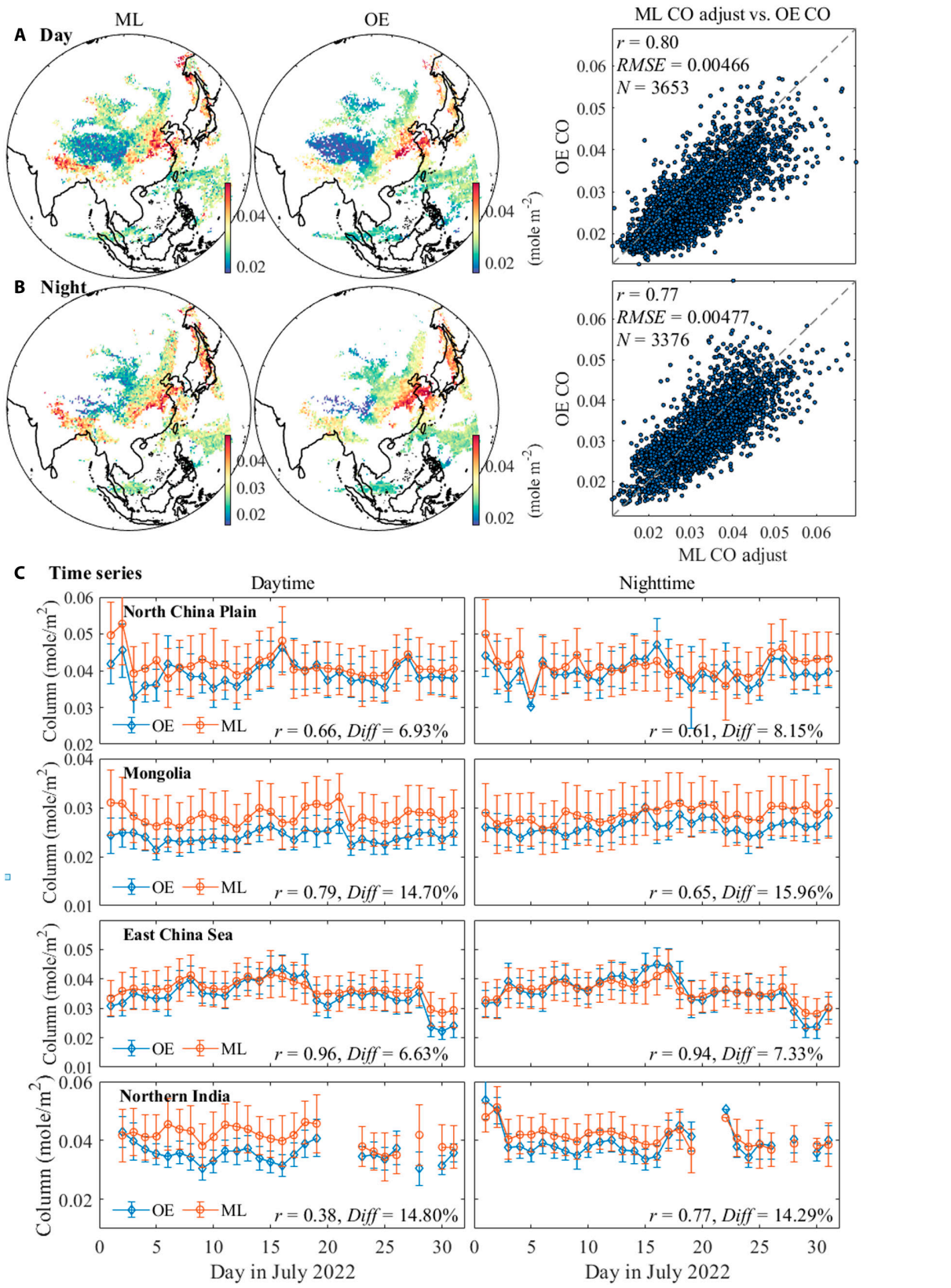

Fig. 5. The spatial and temporal comparisons of GIIRS CO columns retrieved by ML and OE methods. (A) Spatial distribution and scatterplot of GIIRS-ML and GIIRS-OE CO columns during daytime at a unit time resolution on 2022 July 7 (10:00 to 11:59 Beijing time). The values in the scatterplot are the 0.5° × 0.5° grid means matched by GIIRS-ML and GIIRS- GIIRS-OE. (B) Same as (A) but represents the night observation on 2022 July 7 (20:00 to 21:59 Beijing time). There may be slight differences between ML and OE in the spatial distribution due to differences in data preprocessing (e.g., cloud screen) and post-filtering mechanisms. (C) Comparison of the daily average of GIIRS-ML and GIIRS-OE columns in 4 representative regions in July 2022. Here, the column unit is converted from molecules/cm^2 to mole/m^2 via Avogadro's constant to be consistent with Zeng et al. [24].

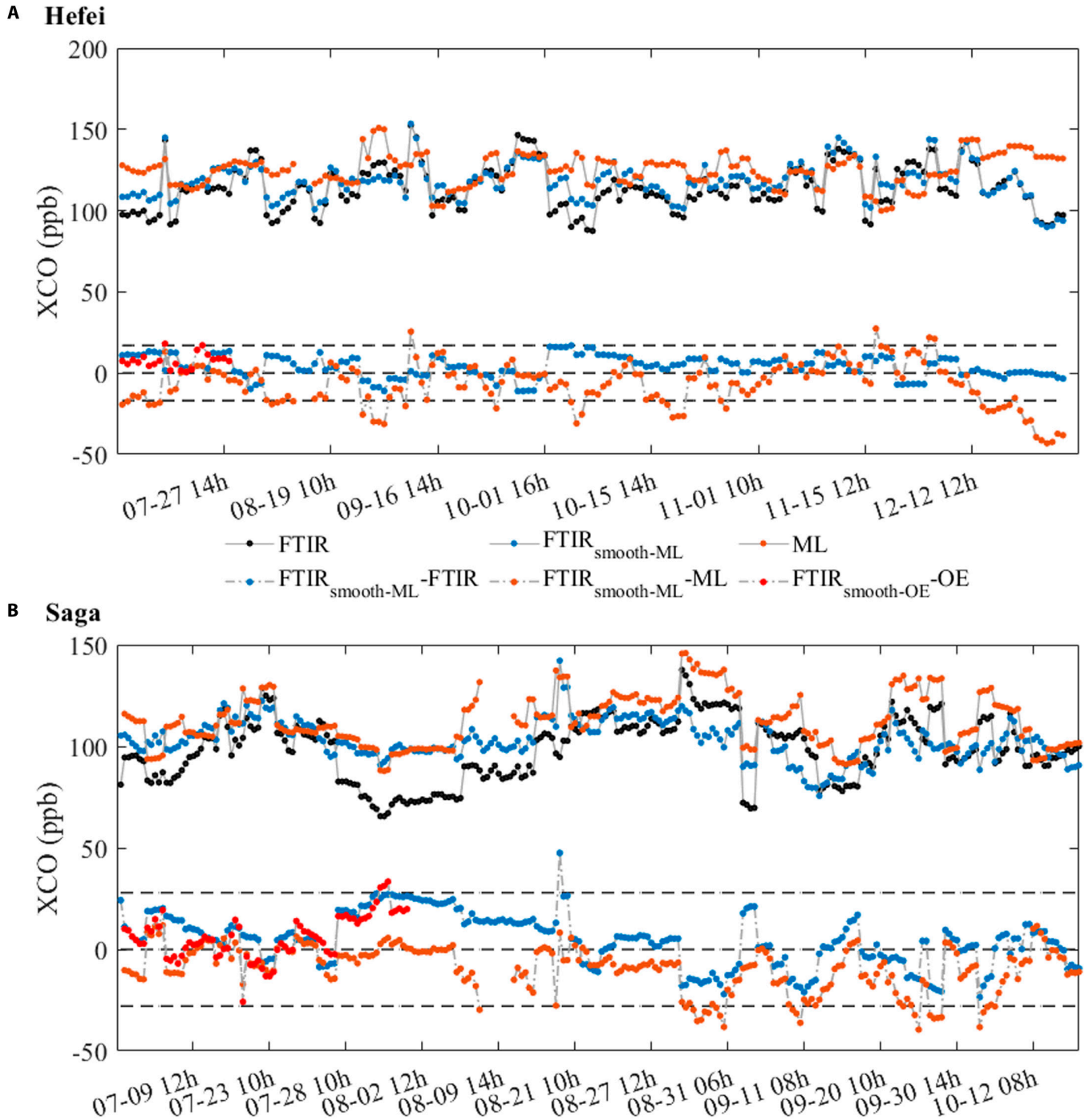

Fig. 6. The evaluation of GIIRS-ML and GIIRS-OE retrieval results with ground-based FTIR measurements at the (A) Hefei and (B) Saga sites. The legend shows that each subfigure contains 3 solid lines and 3 dashed lines. Among the 3 solid lines, the one marked with black circles is the 2-h average FTIR XCO, the one marked with blue circles represents the result of smoothing FTIR XCO based on the ML CO reference profile, and the one marked with orange circles represents GIIRS-ML retrieval results. Among the 3 dotted lines, the one marked with blue circles is the difference between the FTIR XCO and smoothed XCO using the ML CO reference profile. The one marked with orange circles shows the difference between smoothed FTIR and GIIRS-ML XCO. The one marked with red circles represents the difference between the GIIRS-OE XCO and FTIR XCO smoothed by the OE prior profile. The 2 horizontal dotted lines above and below the horizontal dotted line with the ordinate of 0 represent the greatest impact of profile smoothing on FTIR after excluding extreme values. Note: OE results are only available for July 2022, and ground-based FTIR measurements are not continuous.

GIIRS-ML columns are also marked in Fig. 5C. The differences between the 2 datasets are usually less than 8% in the North China Plain and the East China Sea. In Mongolia and northern India, the differences between the 2 datasets are about 14 to 15%, which is within the influence of profile shape in the ML training set. In addition, the comparison between GIIRS-OE and IASI products also shows similar performance (as shown in figure 14 of Zeng et al. [24]). There are larger differences between the 2 datasets in Mongolia and northern India. In future work, optimizing the profile shape in the ML training set and introducing the average kernel can reduce the differences between different datasets.

Evaluation with FTIR measurements

The comparisons in the previous section demonstrate the good spatial and temporal consistency between GIIRS-ML and GIIRS-OE columns, and the differences between them are within the influence level of the reference or prior profiles. This section provides a preliminary evaluation of the GIIRS-ML and GIIRS-OE columns using CO measurements from 2 available ground-based FTIR sites (shown in Fig. S15) within the GIIRS scan region and the period after July 2022. As of the submission date of this manuscript, the data of the Hefei site have been updated to 2022 December 19, and the Saga site has been updated to 2022 October 14. We averaged the FTIR measurements every 2 h and then matched them to the GIIRS-ML and GIIRS-OE columns within 2° and 8 h for comparison. Since the surface altitudes of GIIRS measurements within 2° are not the same as that of the FTIR site, we adapted the GIIRS columns according to the FTIR surface altitude [58,80]. FTIR provides measurements as the column-averaged dry air mole fractions XCO, so we convert GIIRS-OE and GIIRS-ML columns to XCO by dividing by the dry air column density derived from co-located ECMWF pressure fields [80]. According to the official instructions of TCCON (https://tccon-wiki.caltech.edu/Main/AuxiliaryDataGGG2020), the prior profiles and average kernels of FTIR need to be considered when comparing with other products. Therefore, we smooth the XCO of FTIR with the profiles adopted in OE and ML methods, respectively, following the instructions:

$$c_{smooth} = c_a + \mathbf{a}^T\left(x - x_a\right) \tag{6}$$

where c_a is the TCCON XCO prior, x_a is the TCCON CO prior wet mole fraction profile, x is the wet mole fraction profile in OE or ML, and **a** is a vector that is an element-wise product of the TCCON averaging kernel and integration operator provided in the TCCON product.

In Fig. 6, the results before and after smoothing FTIR using the ML reference profile once again prove that the prior profile considerably impacts the retrieval results. In addition, most of the time, using the ML reference profile to smooth the FTIR XCO makes the retrieval results of FTIR and ML closer, which reflects the necessity of considering the profile and average kernel when comparing products of different instruments or algorithms. Moreover, profile smoothing does not change the variation trend of FTIR XCO in time series; GIIRS-ML and FTIR XCO show the same trend in each period. The differences between GIIRS-ML and GIIRS-OE and the smoothed FTIR XCO are also within the level that the profile can influence. However, in December at Hefei station, although GIIRS-ML and FTIR XCO showed a consistent trend, the differences were relatively large. That requires further improvements to the ML algorithm and the collection of more ground measurements for further evaluation in the future.

Diel cycle of CO

As the world's first GEO hyperspectral thermal infrared sensor, GIIRS has the unique advantage of performing high temporal resolution observations during the daytime and nighttime. Considering that CO is long-lived, large outflows are observable over the ocean, particularly from eastern China and Southeast Asia (as shown in the following cases). GIIRS observations are valuable for monitoring the long-range transport of anthropogenic pollutants and biomass burning emissions.

Figure 7 shows the GIIRS-ML CO columns on 2022 September 5 and 2023 April 18, respectively. On that day in September 2022, there were obvious regions with high CO concentrations, including the North China Plain and the Pearl River Delta, dotted with densely populated large cities and vast agricultural areas. In these high-value areas, CO concentrations are higher during the daytime and relatively lower at nighttime. In addition, there are high concentrations in the ocean near the Pearl River Delta with the same diurnal variation, which should relate to the diffusion of pollutants. On that day in April 2023, GIIRS observed widespread high concentrations of CO over land in Southeast Asia, as well as in the ocean regions of Southeast Asia and eastern China. Furthermore, there are obvious long-distance transports of CO over the ocean. For example, in the ocean region of eastern China, the CO concentration is low at 8:00 AM during the daytime, then gradually increases in the following hours, and then reaches and maintains a peak value at nighttime. Similar transport exists in the ocean region of eastern India, but its peak value is only held between 4:00 and 8:00 PM. The CO concentration over land in Southeast Asia shows significant diurnal variations related to the land–ocean transport of pollutants.

Monthly variation of CO

To verify the robustness of the ML method, we retrieved all GIIRS cloud-free measurements from July 2022 to June 2023 and evaluated the reliability of the GIIRS-ML columns with the operational CO products of the MetOp-B/IASI. Figure S16 shows the unfiltered GIIRS-ML CO columns, which show the spatial distribution and monthly variation consistent with the IASI CO columns (Fig. 8), although there are large differences in the scanning frequency between IASI and GIIRS over the region. Specifically, in the summer of July and August 2022 over the land region, the major CO hotspots are the North China Plain, northern India, and Pakistan. In July, there is high CO caused by wildfires in the Siberia region. In the following autumn, from September to November 2022, the hotspots gradually moved southward to the Pearl River Delta and eastern India, with a brief peak in September. In early winter of December 2022, the hotspots are still in the Pearl River Delta and then gradually spread to the North China Plain and Southeast Asia. Over the ocean region, there is an extensive CO transfer belt in March and April 2023.

Figure 9 shows the post-filtered GIIRS-ML CO columns. As discussed in the "Retrieval uncertainty estimation and post-filtering mechanism" section, the strict post-filtering mechanism filters out many winter measurements at northern latitudes, which is consistent with attempts to retrieve CO from GIIRS on a certain day in winter based on the OE method (as shown in section 7.1 and figure S12 of Zeng et al. [24]). This is because the measurement noise of GIIRS in northern latitudes is significantly higher under unfavorable observation conditions in winter. It should be noted that under the $0.5 \times 0.5°$ grid monthly average, especially over the ocean region in March and April 2023, banding effects seem to be related to the GIIRS longitude direction scanning (see Fig. S1). However, we did not find any obvious banding effect after observing the retrieval results at unit time resolution for the whole year from July 2022 to June 2023 (e.g., Fig. 7). Therefore, the above banding effect appearing under the monthly average should be caused by time accumulation, and the impact on the application of GIIRS advantages such as hour-level CO emission and transport research can be ignored.

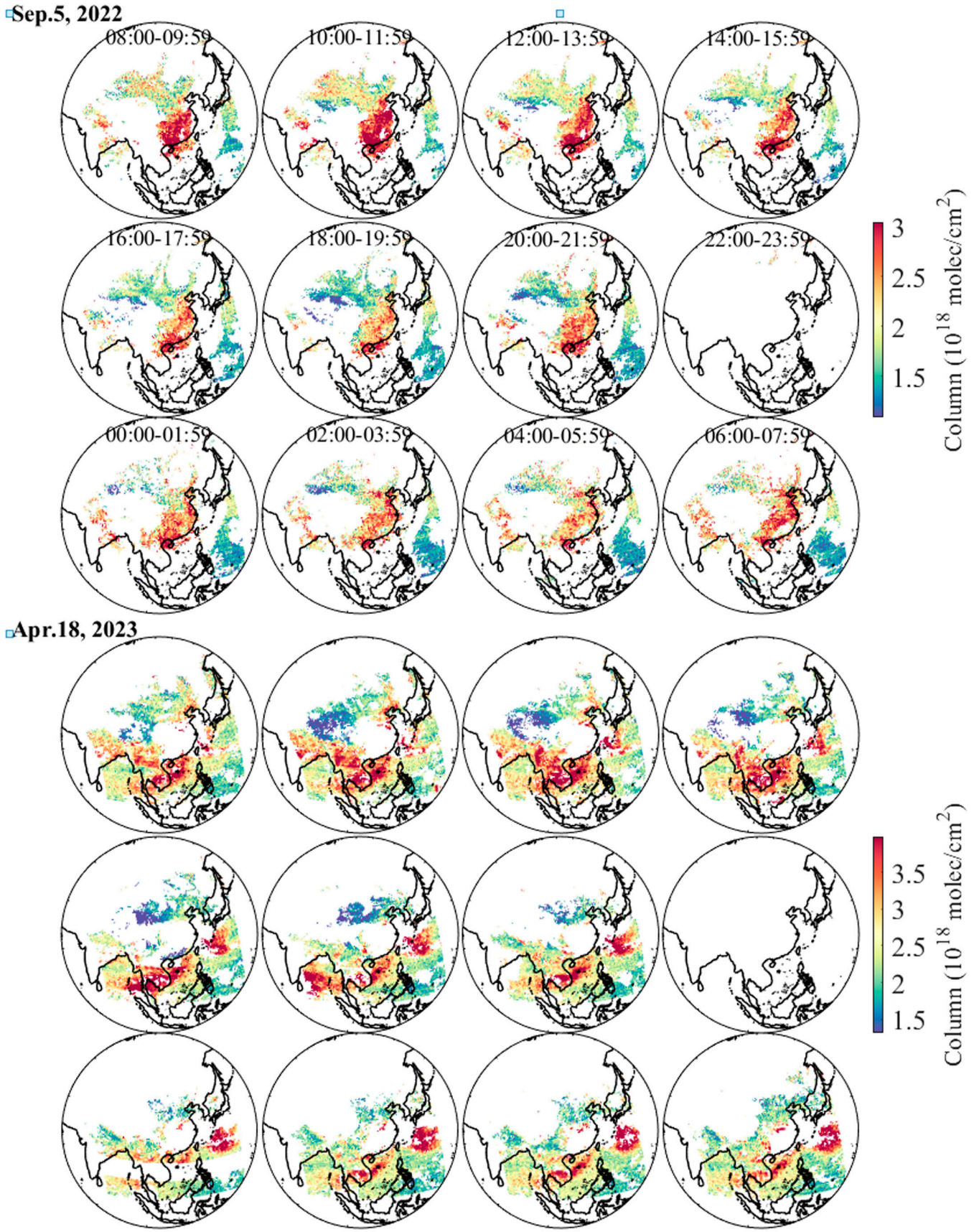

Fig. 7. The post-filtered GIIRS-CO column on 2022 September 5 and 2023 April 18. The figure is drawn with the unit time resolution of GIIRS at a spatial resolution of 0.5 × 0.5°, and the marked time is Beijing time. There are fewer observations from 10:00 to 11:59 PM. During the 2 dates selected here, there are almost no observations.

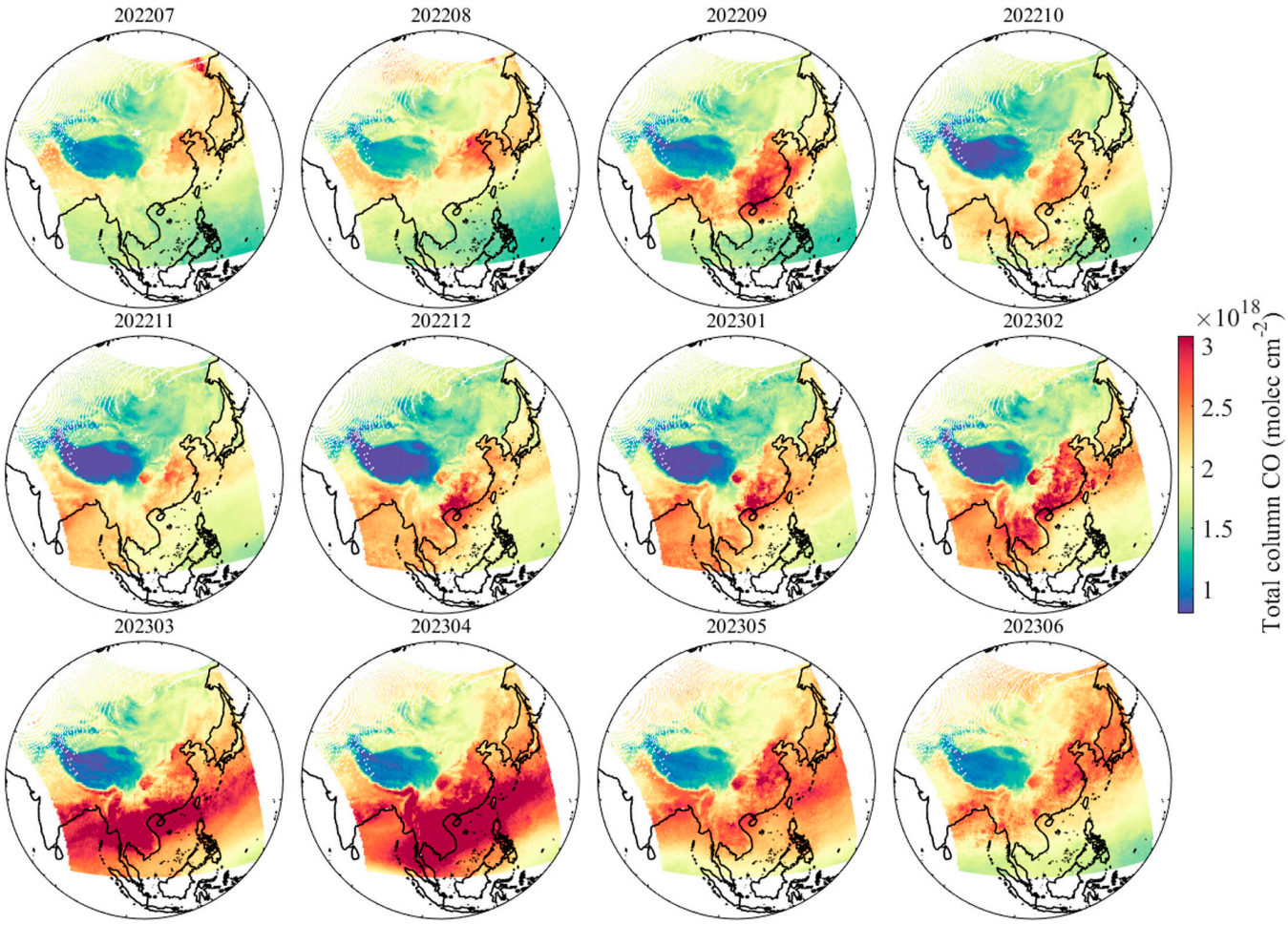

Fig. 8. The IASI CO columns from July 2022 to June 2023. Figures are plotted as monthly averages every 0.5 × 0.5°.

Conclusion

GIIRS is the only GEO hyperspectral thermal infrared sensor so far with the ability to continuously detect hourly CO in East Asia during the daytime and nighttime. Based on the analysis of CO spectral sensitivity and GIIRS measurement performance, this study found that the BTD extracted from the CO absorption peak and valley channels of GIIRS can robustly characterize the distribution and variation of CO. Subsequently, the ML model trained by the RF method can reliably convert BTD and auxiliary parameters into CO columns. From July 2022 to June 2023, the RF model for each month reproduced at least 97.77% and 98.49% of the CO column variance in the land and ocean training sets, and the relative uncertainty of the RF model is generally less than 10% at columns greater than 0.5×10^{18} molecules/cm^2. We retrieved GIIRS clear-sky measurements for a whole year based on the RF models and estimated the absolute uncertainty of the retrieved column and the contribution of each source based on the error propagation theory. Under favorable observation conditions in July 2022, the uncertainty contributed by NEdT usually accounts for more than 90% of the total uncertainty, reflecting that the absolute uncertainty of the GIIRS-ML column is dominated by instrument measurement noise. By observing thousands of unit time GIIRS-ML retrieval results and influencing factors, we found that the ratio of NEdT to BTD is the optimal post-filtering basis.

We performed the spatial and temporal comparisons between the GIIRS-ML and optimal estimate retrieved (GIIRS-OE) columns. GIIRS-ML and GIIRS-OE show the same spatial distribution in the daytime and nighttime scenes, with correlation coefficients of 0.80 and 0.77, respectively. GIIRS-ML and GIIRS-OE found anthropogenic sources in the North China Plain and wildfire emissions in the Siberian. In the 4 representative regions, the GIIRS-ML and GIIRS-OE columns show consistent daily variations during the daytime and nighttime. The correlation coefficients between the 2 during the daytime and nighttime are highest in the East China Sea, reaching 0.96 and 0.94. In North China Plain, Mongolia, and northern India, the correlation coefficients are usually between 0.61 and 0.79. GIIRS-ML also shows a consistent variation trend in each period with the 2 ground-based FTIR measurements in Hefei and Saga. In the 2 cases on 2022 September 5 and 2023 April 18, the diurnal variations of GIIRS-ML columns reflect the advantages of GIIRS in monitoring hourly CO emission and short-term pollutant diffusion. The monthly GIIRS-ML column distributions for the whole year from July 2022 to June 2023 reflect the value of GIIRS in investigating the long-distance transport of anthropogenic pollutants across land and ocean.

This study shows that this novel ML approach can reliably retrieve CO columns from GIIRS, avoiding the complex iterative process of traditional OE, and can theoretically be applied to

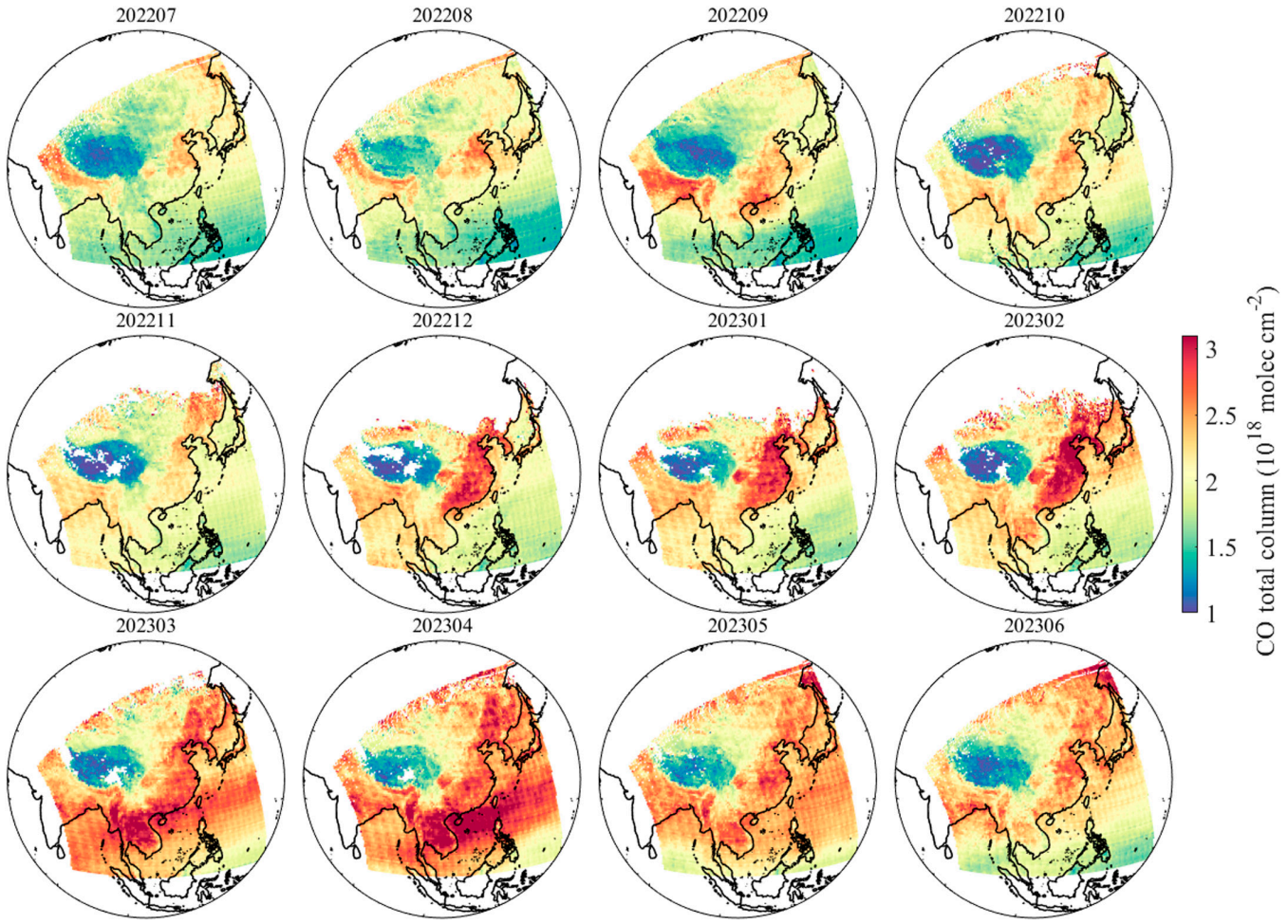

Fig. 9. The post-filtered GIIRS-ML CO columns from July 2022 to June 2023. Figures are plotted as monthly averages every 0.5 × 0.5°. The original GIIRS-ML columns without post-filtering are shown in Fig. S16.

other similar LEO sensors. We roughly estimated the retrieval speed of ML and OE using the same local computing resources (1 CPU core). In the code, we process a pre-extracted GIIRS file with unit time resolution each time. The ML method can process 4,231 files from July 2022 to June 2023 within 40 h, exceeding 42.5 million measurements. However, the OE method requires iterative retrieval for each measurement and can only process about 0.25 million measurements within 40 h. Therefore, ML has great advantages in retrieval efficiency, but the approach still needs further improvements to achieve operational retrieval. In addition to optimizing the selection of reference profiles and introducing average kernels discussed in the "Comparison of CO between ML and OE method" section, finding an alternative to BTD as an index to characterize CO spectral features is meaningful. Specifically, this study expects to extract the spectral features by visualizing CO distribution (i.e., BTD). However, we have to use only a few spectral channels due to the radiance contamination of some GIIRS channels or the accumulation of measurement errors. In the future, using all channels that are sensitive to CO and have little impact from interfering molecules as model inputs may suppress noise and improve the stability of the retrieval results. Furthermore, different spectral channels are sensitive to different altitude layers, so they also have the potential to retrieve the height-resolved CO profile.

Acknowledgments

We are grateful to the team of GIIRS and the National Satellite Meteorological Center (NSMC; http://www.nsmc.org.cn/nsmc/en/home/index.html) for providing open access to the GIIRS data. We are grateful to the TCCON science team. The TCCON data were obtained from the TCCON Data Archive hosted by CaltechDATA at https://tccondata.org. The authors would like to thank HKUST Fok Ying Tung Research Institute and National Supercomputing Center in Guangzhou Nansha Sub-center for providing high-performance computational resources.
Funding: The work is supported by the Hong Kong Research Grants Council (26304921, 16306224) and Hong Kong Environment and Conservation Fund (78-2019, 13-2022). C.Z. and M.Z. are supported by the Strategic Priority Research Program of the Chinese Academy of Sciences (grant XDB41000000) and the USTC Research Funds of the Double First-Class Initiative.
Author contributions: Z.L. designed and performed this study and wrote the original draft. D.G. supervised this study, provided funding acquisition, and reviewed the manuscript. M.Z., N.Y., Y.Y., J.L., and R. Liu provided support for the methodology. C.Z., R. Li, Q.W., and Y.Z. supervised this study and reviewed the manuscript. X.L. and X.C. downloaded and collected the data required for this study.

Competing interests: The authors declare that they have no competing interests.

Data Availability

The core code and data produced by this work are available at https://doi.org/10.5281/zenodo.11178521.

Supplementary Materials

Figs. S1 to S16
Table S1

References

1. Badr O, Probert SD. Carbon monoxide concentration in the Earth's atmosphere. *Appl Energy*. 1994;49(2):99–143.
2. Holloway T, Levy H II, Kasibhatla P. Global distribution of carbon monoxide. *J Geophys Res Atmos*. 2000;105(D10): 12123–12147.
3. Bergamaschi P, Hein R, Heimann M, Crutzen PJ. Inverse modeling of the global CO cycle: 1. Inversion of CO mixing ratios. *J Geophys Res Atmos*. 2000;105(D2):1909–1927.
4. Duncan BN, Logan JA. Model analysis of the factors regulating the trends and variability of carbon monoxide between 1988 and 1997. *Atmos Chem Phys*. 2008;8(24):7389–7403.
5. Lelieveld J, Gromov S, Pozzer A, Taraborrelli D. Global tropospheric hydroxyl distribution, budget and reactivity. *Atmos Chem Phys*. 2016;16(19):12477–12493.
6. Shindell DT, Faluvegi G, Koch DM, Schmidt GA, Unger N, Bauer SE. Improved attribution of climate forcing to emissions. *Science*. 2009;326(5953):716–718.
7. Turquety S, Hurtmans D, Hadji-Lazaro J, Coheur P-F, Clerbaux C, Josset D, Tsamalis C. Tracking the emission and transport of pollution from wildfires using the IASI CO retrievals: Analysis of the summer 2007 Greek fires. *Atmos Chem Phys*. 2009;9(14):4897–4913.
8. Buchholz RR, Worden HM, Park M, Francis G, Deeter MN, Edwards DP, Emmons LK, Gaubert B, Gille J, Martínez-Alonso S, et al. Air pollution trends measured from Terra: CO and AOD over industrial, fire-prone, and background regions. *Remote Sens Environ*. 2021;256:Article 112275.
9. Worden HM, Deeter MN, Frankenberg C, George M, Nichitiu F, Worden J, Aben I, Bowman KW, Clerbaux C, Coheur PF, et al. Decadal record of satellite carbon monoxide observations. *Atmos Chem Phys*. 2013;13(2):837–850.
10. Deeter MN, Edwards DP, Francis GL, Gille JC, Mao D, Martínez-Alonso S, Worden HM, Ziskin D, Andreae MO. Radiance-based retrieval bias mitigation for the MOPITT instrument: The version 8 product. *Atmos Meas Tech*. 2019;12(8):4561–4580.
11. McMillan WW, Barnet C, Strow L, Chahine MT, McCourt ML, Warner JX, Novelli PC, Korontzi S, Maddy ES, Datta S. Daily global maps of carbon monoxide from NASA's Atmospheric Infrared Sounder. *Geophys Res Lett*. 2005;32(11).
12. Rinsland CP, Luo M, Logan JA, Beer R, Worden H, Kulawik SS, Rider D, Osterman G, Gunson M, Eldering A, et al. Nadir measurements of carbon monoxide distributions by the Tropospheric Emission Spectrometer instrument onboard the Aura Spacecraft: Overview of analysis approach and examples of initial results. *Geophys Res Lett*. 2006;33(22).
13. Hurtmans D, Coheur P-F, Wespes C, Clarisse L, Scharf O, Clerbaux C, Hadji-Lazaro J, George M, Turquety S. FORLI radiative transfer and retrieval code for IASI. *J Quant Spectrosc Radiat Transf*. 2012;113(11):1391–1408.
14. Illingworth SM, Remedios JJ, Boesch H, Moore DP, Sembhi H, Dudhia A, Walker JC. ULIRS, an optimal estimation retrieval scheme for carbon monoxide using IASI spectral radiances: Sensitivity analysis, error budget and simulations. *Atmos Meas Tech*. 2011;4(2):269–288.
15. Fu D, Bowman KW, Worden HM, Natraj V, Worden JR, Yu S, Veefkind P, Aben I, Landgraf J, Strow L, et al. High-resolution tropospheric carbon monoxide profiles retrieved from CrIS and TROPOMI. *Atmos Meas Tech*. 2016;9(6):2567–2579.
16. Gambacorta A, Barnet C, Wolf W, King T, Maddy E, Strow L, Xiong X, Nalli N, Goldberg M. An experiment using high spectral resolution CrIS measurements for atmospheric trace gases: Carbon monoxide retrieval impact study. *IEEE Geosci Remote Sens Lett*. 2014;11(9):1639–1643.
17. Buchwitz M, De Beek R, Bramstedt K, Noël S, Bovensmann H, Burrows JP. Global carbon monoxide as retrieved from SCIAMACHY by WFM-DOAS. *Atmos Chem Phys*. 2004;4(7):1945–1960.
18. Frankenberg C, Platt U, Wagner T. Retrieval of CO from SCIAMACHY onboard ENVISAT: Detection of strongly polluted areas and seasonal patterns in global CO abundances. *Atmos Chem Phys*. 2005;5(6):1639–1644.
19. Borsdorff T, Aan de Brugh J, Hu H, Aben I, Hasekamp O, Landgraf J. Measuring carbon monoxide with TROPOMI: First results and a comparison with ECMWF-IFS analysis data. *Geophys Res Lett*. 2018;45(6):2826–2832.
20. Landgraf J, aan de Brugh J, Scheepmaker R, Borsdorff T, Hu H, Houweling S, Butz A, Aben I, Hasekamp O. Carbon monoxide total column retrievals from TROPOMI shortwave infrared measurements. *Atmos Meas Tech*. 2016;9(10): 4955–4975.
21. Noël S, Reuter M, Buchwitz M, Borchardt J, Hilker M, Schneising O, Bovensmann H, Burrows JP, Di Noia A, Parker RJ, et al. Retrieval of greenhouse gases from GOSAT and GOSAT-2 using the FOCAL algorithm. *Atmos Meas Tech*. 2022;15(11):3401–3437.
22. Yang J, Zhang Z, Wei C, Lu F, Guo Q. Introducing the new generation of Chinese geostationary weather satellites, Fengyun-4. *Bull Am Meteorol Soc*. 2017;98:1637–1658.
23. Niu Z, Zhang L, Han Y, Dong P, Huang W. Performances between the FY-4A/GIIRS and FY-4B/GIIRS long-wave infrared (LWIR) channels under clear-sky and all-sky conditions. *Q J R Meteorol Soc*. 2023;149(754):1612–1628.
24. Zeng Z-C, Lee L, Qi C. Diurnal carbon monoxide observed from a geostationary infrared hyperspectral sounder: First result from GIIRS on board FengYun-4B. *Atmos Meas Tech*. 2023;16(12):3059–3083.
25. Maahn M, Turner DD, Löhnert U, Posselt DJ, Ebell K, Mace GG, Comstock JM. Optimal estimation retrievals and their uncertainties: What every atmospheric scientist should know. *Bull Am Meteorol Soc*. 2020;101:E1512–E1523.
26. Rodgers CD. *Inverse methods for atmospheric sounding*. Oxford (UK): World Scientific; 2000.
27. De Wachter E, Barret B, Le Flochmoën E, Pavelin E, Matricardi M, Clerbaux C, Hadji-Lazaro J, George M, Hurtmans D, Coheur P-F, et al. Retrieval of MetOp-A/IASI CO profiles and validation with MOZAIC data. *Atmos Meas Tech*. 2012;5(11):3271–3301.

28. Liu X, Chance K, Sioris CE, Spurr RJD, Kurosu TP, Martin RV, Newchurch MJ. Ozone profile and tropospheric ozone retrievals from the Global Ozone Monitoring Experiment: Algorithm description and validation. *J Geophys Res Atmos*. 2005;110.
29. George M, Clerbaux C, Hurtmans D, Turquety S, Coheur P-F, Pommier M, Hadji-Lazaro J, Edwards DP, Worden H, Luo M, et al. Carbon monoxide distributions from the IASI/METOP mission: Evaluation with other space-borne remote sensors. *Atmos Chem Phys*. 2009;9(21):8317–8330.
30. Franco B, Clarisse L, Stavrakou T, Müller J-F, Van Damme M, Whitburn S, Hadji-Lazaro J, Hurtmans D, Taraborrelli D, Clerbaux C, et al. A general framework for global retrievals of trace gases from IASI: Application to methanol, formic acid, and PAN. *J Geophys Res Atmos*. 2018;123:13963–13984.
31. Guo Q, Yang J, Wei C, Chen B, Wang X, Han C, Hui W, Xu W, Wen R, Liu Y. Spectrum calibration of the first hyperspectral infrared measurements from a geostationary platform: Method and preliminary assessment. *Q J R Meteorol Soc*. 2021;147(736):1562–1583.
32. Yin R, Han W, Gao Z, Di D. The evaluation of FY4A's geostationary interferometric infrared sounder (GIIRS) long-wave temperature sounding channels using the GRAPES global 4D-Var. *Q J R Meteorol Soc*. 2020;146(728):1459–1476.
33. Belgiu M, Drăguț L. Random forest in remote sensing: A review of applications and future directions. *ISPRS J Photogramm Remote Sens*. 2016;114:24–31.
34. Yuan Q, Shen H, Li T, Li Z, Li S, Jiang Y, Xu H, Tan W, Yang Q, Wang J, et al. Deep learning in environmental remote sensing: Achievements and challenges. *Remote Sens Environ*. 2020;241:Article 111716.
35. Whitburn S, Van Damme M, Clarisse L, Bauduin S, Heald CL, Hadji-Lazaro J, Hurtmans D, Zondlo MA, Clerbaux C, Coheur P-F. A flexible and robust neural network IASI-NH3 retrieval algorithm. *J Geophys Res Atmos*. 2016;121(11):6581–6599.
36. Clarisse L, Van Damme M, Hurtmans D, Franco B, Clerbaux C, Coheur P-F. The diel cycle of NH3 observed from the FY-4A geostationary interferometric infrared sounder (GIIRS). *Geophys Res Lett*. 2021;48(14):e2021GL093010.
37. Franco B, Clarisse L, Van Damme M, Hadji-Lazaro J, Clerbaux C, Coheur P-F. Ethylene industrial emitters seen from space. *Nat Commun*. 2022;13(1):6452.
38. Franco B, Clarisse L, Stavrakou T, Müller J-F, Taraborrelli D, Hadji-Lazaro J, Hannigan JW, Hase F, Hurtmans D, Jones N, et al. Spaceborne measurements of formic and acetic acids: A global view of the regional sources. *Geophys Res Lett*. 2020;47(4):e2019GL086239.
39. Franco B, Clarisse L, Stavrakou T, Müller J-F, Pozzer A, Hadji-Lazaro J, Hurtmans D, Clerbaux C, Coheur P-F. Acetone atmospheric distribution retrieved from space. *Geophys Res Lett*. 2019;46(5):2884–2893.
40. Van Damme M, Clarisse L, Franco B, Sutton MA, Erisman JW, Kruit RW, Van Zanten M, Whitburn S, Hadji-Lazaro J, Hurtmans D. Global, regional and national trends of atmospheric ammonia derived from a decadal (2008–2018) satellite record. *Environ Res Lett*. 2021;16(5):Article 055017.
41. Wells KC, Millet DB, Payne VH, Vigouroux C, Aquino CAB, De Mazière M, de Gouw JA, Graus M, Kurosu T, Warneke C, et al. Next-generation isoprene measurements from space: Detecting daily variability at high resolution. *J Geophys Res Atmos*. 2022;127:e2021JD036181.
42. Walker JC, Dudhia A, Carboni E. An effective method for the detection of trace species demonstrated using the MetOp infrared atmospheric sounding interferometer. *Atmos Meas Tech*. 2011;4(8):1567–1580.
43. Clarisse L, Clerbaux C, Franco B, Hadji-Lazaro J, Whitburn S, Kopp AK, Hurtmans D, Coheur P-F. A decadal data set of global atmospheric dust retrieved from IASI satellite measurements. *J Geophys Res Atmos*. 2019;124(3):1618–1647.
44. Clarisse L, Coheur P-F, Prata AJ, Hurtmans D, Razavi A, Phulpin T, Hadji-Lazaro J, Clerbaux C. Tracking and quantifying volcanic SO2 with IASI, the September 2007 eruption at Jebel at Tair. *Atmos Chem Phys*. 2008;8(24):7723–7734.
45. Clarisse L, Clerbaux C, Dentener F, Hurtmans D, Coheur P-F. Global ammonia distribution derived from infrared satellite observations. *Nat Geosci*. 2009;2:479–483.
46. Coheur P-F, Clarisse L, Turquety S, Hurtmans D, Clerbaux C. IASI measurements of reactive trace species in biomass burning plumes. *Atmos Chem Phys*. 2009;9(15):5655–5667.
47. Fu D, Millet DB, Wells KC, Payne VH, Yu S, Guenther A, Eldering A. Direct retrieval of isoprene from satellite-based infrared measurements. *Nat Commun*. 2019;10:3811.
48. Razavi A, Karagulian F, Clarisse L, Hurtmans D, Coheur PF, Clerbaux C, Müller JF, Stavrakou T. Global distributions of methanol and formic acid retrieved for the first time from the IASI/MetOp thermal infrared sounder. *Atmos Chem Phys*. 2011;11(2):857–872.
49. Wells KC, Millet DB, Payne VH, Deventer MJ, Bates KH, de Gouw JA, Graus M, Warneke C, Wisthaler A, Fuentes JD. Satellite isoprene retrievals constrain emissions and atmospheric oxidation. *Nature*. 2020;585(7824):225–233.
50. Li L, Ni Z, Qi C, Yang L, Han C. Pre-launch radiometric calibration of geostationary interferometric infrared sounder on FengYun-4B satellite. *Acta Opt Sin*. 2022;42(6):0630001.
51. Lai R, Teng S, Yi B, Letu H, Min M, Tang S, Liu C. Comparison of cloud properties from Himawari-8 and FengYun-4A geostationary satellite radiometers with MODIS cloud retrievals. *Remote Sens*. 2019;11(14):1703.
52. Wang X, Min M, Wang F, Guo J, Li B, Tang S. Intercomparisons of cloud mask products among Fengyun-4A, Himawari-8, and MODIS. *IEEE Trans Geosci Remote Sens*. 2019;57(11):8827–8839.
53. Hersbach H, Bell B, Berrisford P, Hirahara S, Horányi A, Muñoz-Sabater J, Nicolas J, Peubey C, Radu R, Schepers D, et al. The ERA5 global reanalysis. *Q J R Meteorol Soc*. 2020;146(730):1999–2049.
54. Seemann SW, Borbas EE, Knuteson RO, Stephenson GR, Huang H-L. Development of a global infrared land surface emissivity database for application to clear sky sounding retrievals from multispectral satellite radiance measurements. *J Appl Meteorol Climatol*. 2008;47:108–123.
55. Goldberg M, Ohring G, Butler J, Cao C, Datla R, Doelling D, Gärtner V, Hewison T, Iacovazzi B, Kim D, et al. The global space-based inter-calibration system. *Bull Am Meteorol Soc*. 2011;92:467–475.
56. George M, Clerbaux C, Bouarar I, Coheur P-F, Deeter MN, Edwards DP, Francis G, Gille JC, Hadji-Lazaro J, Hurtmans D, et al. An examination of the long-term CO records from MOPITT and IASI: Comparison of retrieval methodology. *Atmos Meas Tech*. 2015;8(1):4313–4328.
57. Illingworth SM, Remedios JJ, Boesch H, Ho S-P, Edwards DP, Palmer PI, Gonzi S. A comparison of OEM CO retrievals from the IASI and MOPITT instruments. *Atmos Meas Tech*. 2011;4(5):775–793.

58. Kerzenmacher T, Dils B, Kumps N, Blumenstock T, Clerbaux C, Coheur P-F, Demoulin P, García O, George M, Griffith DWT, et al. Validation of IASI FORLI carbon monoxide retrievals using FTIR data from NDACC. *Atmos Meas Tech*. 2012;5(11):2751–2761.
59. Klonecki A, Pommier M, Clerbaux C, Ancellet G, Cammas J-P, Coheur P-F, Cozic A, Diskin GS, Hadji-Lazaro J, Hauglustaine DA, et al. Assimilation of IASI satellite CO fields into a global chemistry transport model for validation against aircraft measurements. *Atmos Chem Phys*. 2012;12(10): 4493–4512.
60. Pommier M, Law KS, Clerbaux C, Turquety S, Hurtmans D, Hadji-Lazaro J, Coheur P-F, Schlager H, Ancellet G, Paris J-D, et al. IASI carbon monoxide validation over the Arctic during POLARCAT spring and summer campaigns. *Atmos Chem Phys*. 2010;10(21):10655–10678.
61. Laughner JL, Toon GC, Mendonca J, Petri C, Roche S, Wunch D, Blavier J-F, Griffith DWT, Heikkinen P, Keeling RF, et al. The total carbon column observing network's GGG2020 data version. *Earth Syst Sci Data*. 2023;2023(5):1–86.
62. Wunch D, Toon GC, Sherlock V, Deutscher NM, Liu C, Feist DG, Wennberg PO. *Documentation for the 2014 TCCON Data Release, CaltechDATA*. Oak Ridge (TN): Carbon Dioxide Information Analysis Center, Oak Ridge National Laboratory; 2015.
63. Wunch D, Toon GC, Blavier J-FL, Washenfelder RA, Notholt J, Connor BJ, Griffith DWT, Sherlock V, Wennberg PO. The total carbon column observing network. *Philos Trans R Soc A Math Phys Eng Sci*. 2011;369:2087–2112.
64. Liu C, Wang W, Sun Y, Shang C. TCCON Data from Hefei, China, Release GGG2020R1. TCCON Data Archive, Hosted by CaltechDATA, California Institute of Technology, Pasadena, CA, USA, 2022.
65. Wang W, Tian Y, Liu C, Sun Y, Liu W, Xie P, Liu J, Xu J, Morino I, Velazco VA, et al. Investigating the performance of a greenhouse gas observatory in Hefei, China. *Atmos Chem Phys*. 2017;10(7):2627–2643.
66. Ohyama H, Kawakami S, Tanaka T, Morino I, Uchino O, Inoue M, Sakai T, Nagai T, Yamazaki A, Uchiyama A, et al. Observations of XCO_2 and XCH_4 with ground-based high-resolution FTS at Saga, Japan, and comparisons with GOSAT products. *Atmos Meas Tech*. 2015;8(12):5263–5276.
67. Shiomi K, Kawakami S, Ohyama H, Arai K, Okumura H, Ikegami H, Usami M. TCCON Data from Saga, Japan, Release GGG2020R0. TCCON Data Archive, Hosted by CaltechDATA, California Institute of Technology, Pasadena, CA, USA, 2022.
68. Hocking J, Vidot J, Brunel P, Roquet P, Silveira B, Turner E, Lupu C. A new gas absorption optical depth parameterisation for RTTOV version 13. *Geosci Model Dev*. 2021;14(5): 2899–2915.
69. Saunders R, Hocking J, Turner E, Rayer P, Rundle D, Brunel P, Vidot J, Roquet P, Matricardi M, Geer A, et al. An update on the RTTOV fast radiative transfer model (currently at version 12). *Geosci Model Dev*. 2018;11(7):2717–2737.
70. Pope RJ, Kerridge BJ, Siddans R, Latter BG, Chipperfield MP, Arnold SR, Ventress LJ, Pimlott MA, Graham AM, Knappett DS, et al. Large enhancements in southern hemisphere satellite-observed trace gases due to the 2019/2020 Australian wildfires. *J Geophys Res Atmos*. 2021;126(18):e2021 JD034892.
71. Bauduin S, Clarisse L, Theunissen M, George M, Hurtmans D, Clerbaux C, Coheur P-F. IASI's sensitivity to near-surface carbon monoxide (CO): Theoretical analyses and retrievals on test cases. *J Quant Spectrosc Radiat Transf*. 2017;189: 428–440.
72. Masuda K, Takashima T, Takayama Y. Emissivity of pure and sea waters for the model sea surface in the infrared window regions. *Remote Sens Environ*. 1988;24(2):313–329.
73. Inness A, Ades M, Agustí-Panareda A, Barré J, Benedictow A, Blechschmidt A-M, Dominguez JJ, Engelen R, Eskes H, Flemming J, et al. The CAMS reanalysis of atmospheric composition. *Atmos Chem Phys*. 2019;19(6):3515–3556.
74. Breiman L. Random forests. *Mach learn*. 2001;45:5–32.
75. Van Damme M, Whitburn S, Clarisse L, Clerbaux C, Hurtmans D, Coheur P-F. Version 2 of the IASI NH3 neural network retrieval algorithm: Near-real-time and reanalysed datasets. *Atmos Meas Tech*. 2017;10(12):4905–4914.
76. Salstein DA, Ponte RM, Cady-Pereira K. Uncertainties in atmospheric surface pressure fields from global analyses. *J Geophys Res Atmos*. 2008;113(D14).
77. Gualtieri G. Analysing the uncertainties of reanalysis data used for wind resource assessment: A critical review. *Renew Sust Energ Rev*. 2022;167:Article 112741.
78. Rodgers CD, Connor BJ. Intercomparison of remote sounding instruments. *J Geophys Res Atmos*. 2003;108(D3).
79. Clarisse L, Franco B, Van Damme M, Di Gioacchino T, Hadji-Lazaro J, Whitburn S, Noppen L, Hurtmans D, Clerbaux C, Coheur P. The IASI NH_3 version 4 product: Averaging kernels and improved consistency. *Atmos Meas Tech*. 2023;16(21):5009–5028.
80. Borsdorff T, aan de Brugh J, Hu H, Hasekamp O, Sussmann R, Rettinger M, Hase F, Gross J, Schneider M, Garcia O, et al. Mapping carbon monoxide pollution from space down to city scales with daily global coverage. *Atmos Meas Tech* 2018;11(10):5507–5518.